BNL-223170-2022-JAAM

Manipulating Interfacial Dissolution-Redeposition Dynamics to Resynthesize Electrode Surface Chemistry

A. Hu, S. Hwang

To be published in "ACS Energy Letters"

July 2022

Center for Functional Nanomaterials

Brookhaven National Laboratory

U.S. Department of Energy

USDOE Office of Science (SC), Basic Energy Sciences (BES) (SC-22)

DISCLAIMER

Manipulating Interfacial Dissolution-Redeposition Dynamics to Resynthesize Electrode Surface Chemistry

Anyang Hu,[1] Yuxin Zhang,[1] Fan Yang,[2] Sooyeon Hwang,[3] Sami Sainio,[4,7] Dennis Nordlund,[4] Evan Maxey,[5] Qilin Dai,[6] Jing Gu,[2] Luxi Li,[5]* Feng Lin[1]*

1 Department of Chemistry, Virginia Tech, Blacksburg, VA 24061, USA.

2 Department of Chemistry and Biochemistry, San Diego State University, San Diego, CA, 92181, USA

3 Center for Functional Nanomaterials, Brookhaven National Laboratory, Upton, New York 11973, USA

4 Stanford Synchrotron Radiation Lightsource, SLAC National Accelerator Laboratory, Menlo Park, CA 94025, USA

5 Advanced Photon Source, Argonne National Laboratory, Argonne, IL 60439, USA

6 Department of Chemistry, Physics and Atmospheric Sciences, Jackson State University, Jackson, MS 39217, USA

7 Microelectronics Research Unit, Faculty of Information Technology and Electrical Engineering University of Oulu, P.O. Box. 4500, 90570 Oulu, Finland

*E-mail: fenglin@vt.edu; luxili@anl.gov

Abstract

The solid-liquid electrochemical interface offers a two-dimensional environment for geometrically confined interfacial reactions to tailor electrode surface chemistry under operating conditions. Herein, we demonstrate that the dissolution and redeposition kinetics of transition metal cations, a ubiquitous phenomenon at the electrochemical interface, can be manipulated to regulate the chemical composition and crystal structure of the electrode surface as well as the overall electrochemical performance. Foreign cations (e.g., Ti^{4+}), either added as electrolyte additives or dissolved from surface coatings, can rapidly participate in the electrode dissolution-redeposition process, and facilitate the establishment of the dissolution-redeposition equilibrium. Our work expands the control over the electrochemical reactions at the solid-liquid interface and provides new insights into interfacial studies in electrochemistry and surface science.

TOC

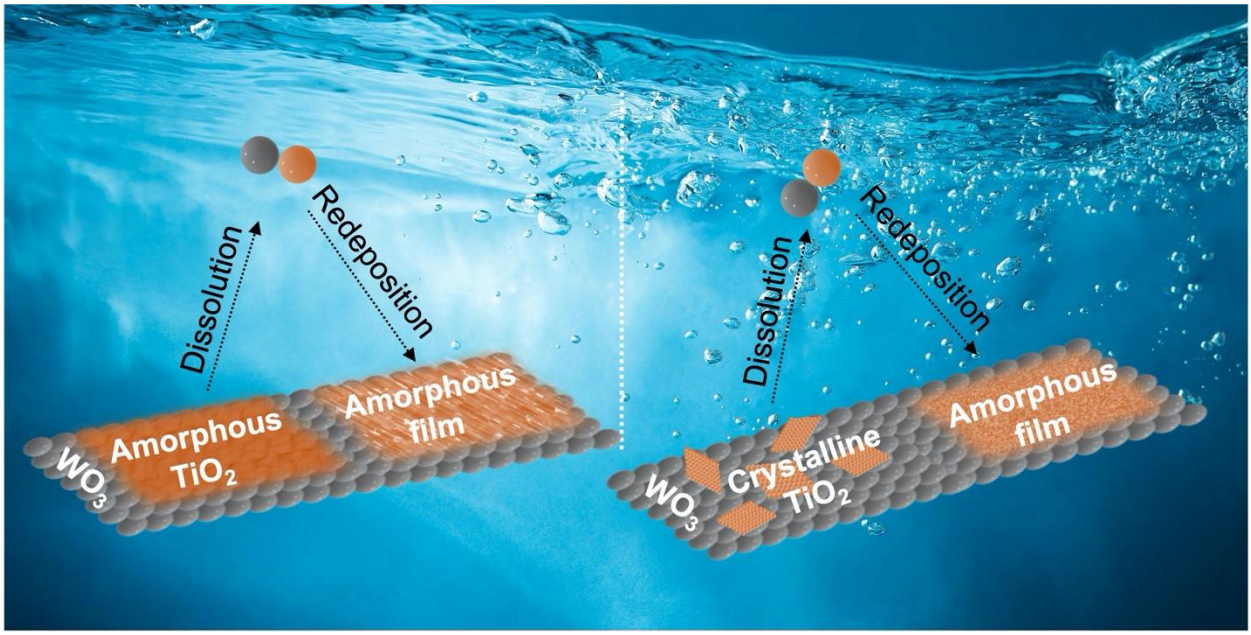
Dissolution
Redeposition
Amorphous TiO_2
Amorphous film
WO_3
Dissolution
Redeposition
Crystalline TiO_2
Amorphous film
WO_3

The research on rechargeable batteries, electrocatalysis, and electrochromics continues to expand, reflecting the growing demand for high-performance electrochemical energy systems.[1] The electrochemical performance of these systems relies on stable interactions between electrodes and electrolytes.[2] Surface coatings have been shown effective in modulating electrode surface chemistry and thus interfacial reactions. [3, 4] These layers act as physical protective barriers to limit side reactions between electrodes and electrolytes, which mitigates electrode dissolution,[5] electrolyte decomposition,[6] parasitic gas evolution,[7] and electrode mechanical degradation.[8] They can also serve as charge transfer promoting agents to accelerate electron and/or ion transport, such as carbon thin layer[9] and solid-electrolyte thin layer[10] on electrode surface.[11, 12] Most studies have focused on improving electrochemical performance using various surface coatings, with little attention paid to the functioning mechanisms or structural evolution of these surface coatings under electrochemical reactions.

The electrochemical interface, where the surface coating is located, is a dynamically reactive environment.[13-16] Maintaining the structural and chemical integrity of thin surface coatings is usually challenging, in part because surface coatings themselves can participate in electrochemical reactions. For example, the rutile-TiO_2 surface coating layer on $Li_4Ti_5O_{12}$ anode contributes to the first discharge capacity and improves anode rate capability.[17] Different thicknesses of SnO_2 surface coatings on Cu substrates can selectively promote the electrochemical reduction of CO_2 to CO or formate.[18] However, how thin surface coatings undergo chemical and structural transformations under electrochemical conditions remains an open question. Exploring the dynamic evolution of

surface coatings will offer new insights into reactive electrochemical interfaces that are ubiquitous in nearly all heterogeneous electrochemical systems involving solid-liquid interfaces.

Here, we investigate how a common surface coating material (TiO_2) transforms and exhibits strong interactions with the proton-intercalation electrode (WO_3). WO_3 electrodes undergo dissolution-redeposition during repeated proton intercalation/deintercalation in the sulfuric acid (H_2SO_4) electrolyte. Including Ti cations in the electrolyte enables Ti cations to participate in such a dynamic process, leading to the *in situ* formation of an amorphous TiO_2 surface layer, which promotes the dissolution-redeposition equilibrium at the electrochemical interface, thus alleviating WO_3 dissolution and modulating the electrode morphology. Such a dynamic evolution can also transform heterogeneous, crystalline TiO_2 islands into a homogenous, amorphous coating layer. This work demonstrates the intertwined dissolution-redeposition dynamics between the oxide surface coating and the electrode in aqueous electrolytes and highlights that the electrochemical interface can be manipulated to resynthesize electrode surface chemistry for enhanced electrochemical performance.

Changing the electrolyte composition can modify the electrode surface structure under electrochemical conditions. Our previous work has illustrated that foreign Fe^{3+} cations in the electrolyte can selectively incorporate into edge sites of the $Ni(OH)_2$ electrocatalyst, resulting in an effective oxygen evolution reaction.[19] Besides, repeated WO_3 dissolution and redeposition can degrade the electrochromic performance of WO_3 electrodes in the H_2SO_4 electrolyte.[20] We conjecture that adding foreign cations to the electrolyte could impact the dissolution-redeposition

dynamics, modulate the WO_3 electrode surface structure, and decelerate the degradation. Here, 0.1 M $TiOSO_4$ is added to 0.5 M H_2SO_4 as the electrolyte to cycle the WO_3 working electrode. In the typical three-electrode configuration, the Pt foil is the counter electrode, and Ag/AgCl is the reference electrode (details in experimental sections). Electrochemical cycling with variable scan rates can reveal the different kinetic behaviors of various cations in electrolytes.[21] Slow cyclic voltammetry (CV) cycling (0.1 mV/s scan rate, **Figure 1a**) of the WO_3 electrode in the 0.1 M $TiOSO_4$ + 0.5 M H_2SO_4 electrolyte is almost irreversible without corresponding anodic currents. However, when under high scan rates (**Figure 1a, the inset**), the CV performance is similar to the one cycled in the 0.5 M H_2SO_4 only electrolyte (**Figure S1**). Therefore, when the WO_3 electrode is cycled at different scan rates in the mixed 0.1 M $TiOSO_4$ + 0.5 M H_2SO_4 electrolyte, there is a significant difference in the kinetics between Ti cations and protons. With slow CV scan rates, irreversible deposition of Ti cations dominates the electrochemical process, while with increasing scan rates, reversible proton intercalation and deintercalation gradually dominate. Thermodynamically, based on the Pourbaix diagram of the Ti-H_2O system, TiO_2 is preferentially formed under our pH (pH=0.6) and potential conditions (0.044 V-0.844 V vs standard hydrogen electrode).[22] After slow CV cycling, Ti L-edge soft-X-ray absorption spectroscopy (s-XAS) of the WO_3 electrode (**Figure 1b**) shows the formation of a nearly amorphous TiO_2 surface layer.[23] Faster CV cycling cannot induce the formation of this TiO_2 surface layer (**Figure S2**), which can further verify the kinetic difference of Ti cations and protons. The pure FTO substrate, with a dense Fluorine-doped Tin Oxide layer, exhibits the same Ti L-edge s-XAS results when cycled in the 0.1 M $TiOSO_4$ + 0.5 M H_2SO_4 electrolyte (**Figure S3**). Therefore, the formation of the amorphous

TiO_2 surface layer is not governed by the nature of the electrode but rather by the electrochemical protocol. The presence of the TiO_2 surface layer can also be validated by scanning transmission electron microscopy-energy dispersive X-ray spectroscopy (STEM-EDS) Ti elemental map (**Figure S4)** and Ti L-edge electron energy loss spectroscopy (EELS) line profile (**Figure S5**). Due to the 5-10 nm WO_3 nanocrystals within the WO_3 electrode and its porous nature,[20] newly formed TiO_2 surface layer is present throughout the electrode. Next, the formation of this TiO_2 surface layer is monitored using *in situ* X-ray fluorescence microscopy (XFM). As a scanning probe technique with high elemental sensitivity, XFM has been used to investigate the structural evolution of the electrode, such as phase segregation, and metal dissolution and redeposition, based on element-sensitive fluorescence signals.[24-26] Using our customized *in situ* XFM electrochemical cell (**Figure 1c**-**1d,** details in experimental sections), with the addition of the 0.1 M $TiOSO_4$ + 0.5 M H_2SO_4 aqueous electrolyte, the new broad Ti-element fluorescence signal at ~ 250 counts/pixel comes from the electrolyte (**Figure 1e**). As slow CV cycling proceeds, since the Ti-element fluorescence signal of the amorphous solid TiO_2 surface layer is stronger than that from the Ti-containing electrolyte, the increasing number of pixels at high Ti-element fluorescence counts/pixel positions represents the gradual deposition of the solid TiO_2 surface layer (**Figure 1e**), which is consistent with the signal buildup in Ti-element XFM images (**Figure 1f**). In the meantime, W elemental distribution curves shift slightly to the left (**Figure S6**), indicating that the W content in the electrode marginally decreased. Therefore, the TiO_2 surface layer can be formed by controlling electrochemical conditions, accompanied by a slight dissolution of the WO_3 electrode.

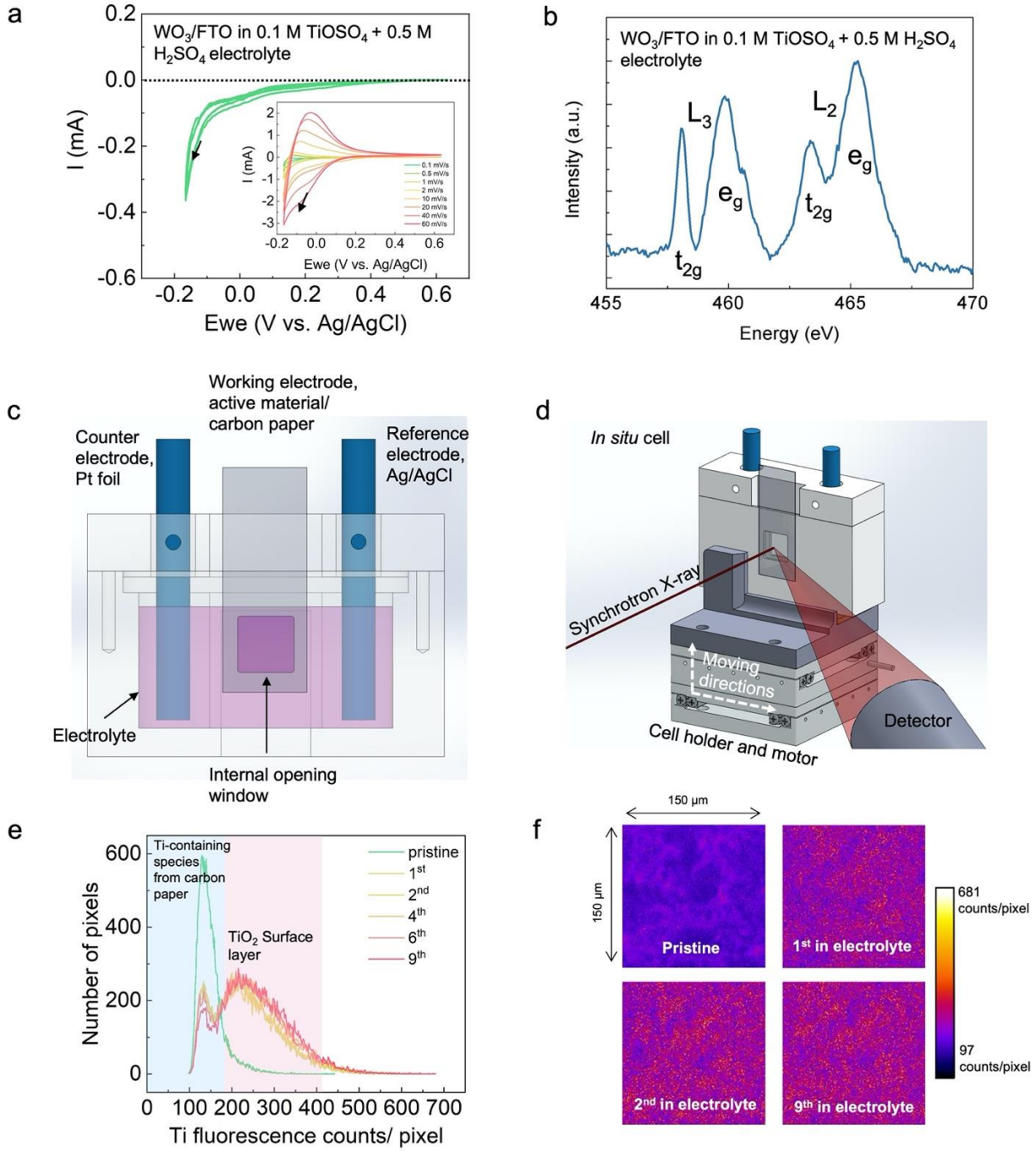

Figure 1 The formation of the amorphous TiO_2 surface layer on the WO_3 electrode surface.

(a) Cyclic voltammetry (CV) of the WO_3/FTO electrode for 3 CV cycles in the 0.1 M $TiOSO_4$ + 0.5 M H_2SO_4 electrolyte at 0.1 mV/s scan rate with -0.165 V-0.635 V vs. Ag/AgCl (3M, NaCl). The inset is the CV curves of the WO_3/FTO electrode in the 0.1 M $TiOSO_4$ + 0.5 M H_2SO_4

electrolyte at various scan rates within the same potential range. The arrow indicates the direction of CV cycling. (b) Ti L-edge s-XAS in the TEY (total electron yield) mode of the WO_3/FTO electrode after 3 CV cycles in the 0.1 M $TiOSO_4$ + 0.5 M H_2SO_4 electrolyte at 0.1 mV/s scan rate with -0.165 V-0.635 V vs. Ag/AgCl (3M, NaCl). No pre-edge features, no splitting of the L_3-e_g subband, and the higher peak intensity of the L_3-e_g subband (compared to the L_3-t_{2g} subband) suggest the amorphous feature of TiO_2. Only the TEY mode is analyzed in s-XAS because the thin thickness of the newly formed TiO_2 surface layer gives the FY (fluorescence yield) mode a relatively noisier signal. (c) The specific structure of the *in situ* XFM electrochemical cell is a three-electrode electrochemical system. Carbon paper is used as the substrate for better X-ray penetration. (d) *In situ* XFM experimental setup in the 2 ID-E beamline at the Advanced Photon Source. More details are in the experimental section. (e) Ti elemental distribution curves of the Ti-element fluorescence counts/pixel (pixel size: 1 μm x 1 μm, X-axis) and the number of pixels (Y-axis) of the WO_3/C electrode during 3 CV cycles in the 0.1 M $TiOSO_4$ + 0.5 M H_2SO_4 electrolyte at 0.5 mV/s scan rate with -0.165 V-0.635 V vs. Ag/AgCl (3M, NaCl). Pristine Ti elemental distribution curve is without the electrolyte, suggesting the existence of Ti-containing species from carbon paper. The 1st Ti elemental distribution curve is the one right after adding 0.1 M $TiOSO_4$ + 0.5 M H_2SO_4 electrolyte, indicating the beginning of slow electrochemical cycling. The subsequent 2nd to the 9th Ti elemental distribution curves show the evolution of Ti elemental distribution during the formation of the TiO_2 surface layer. (f) Ti-element XFM images during the formation of the TiO_2 surface layer in (e), where the color bar on the right represents the absolute Ti-element fluorescence counts in each pixel.

By using *in situ* XFM and pixel-by-pixel quantitative analysis, we can learn more about how the newly formed TiO_2 surface layer interacts with the WO_3 electrode during 3,000 CV cycling in the 0.5 M H_2SO_4 electrolyte for improved electrochemical performance. Higher Coulombic efficiency (**Figure 2a**) and larger optical modulation (**Figure 2b**) can be obtained during 3,000 CV cycling in the 0.5 M H_2SO_4 electrolyte after forming a TiO_2 surface layer at a scan rate of 0.5 mV/s in 0.1 M $TiOSO_4$ + 0.5 M H_2SO_4 electrolyte. The formed amorphous TiO_2 surface layer can be observed at the beginning of the 3,000 CV cycling in the 0.5 M H_2SO_4 electrolyte (**Figure S7**, 1st Ti-element XFM image). The gradual decay of the Ti-element fluorescence signal at high Ti-element fluorescence counts/pixel positions in the Ti elemental distribution curves further confirms the existence and the dissolution of the TiO_2 surface layer (**Figure S8**). Regarding the WO_3 electrode, with the TiO_2 surface layer (**Figure 2c** and **S9**) and without (**Figure S10a** and **S11**), a series of W elemental distribution curves and XFM images can reveal that there is no major net WO_3 dissolution with the TiO_2 surface layer (**Figure 2c**), while the WO_3 electrode without the TiO_2 surface layer has experienced severe net dissolution (**Figure S11**). The suppressed WO_3 dissolution can also be manifested with the ICP-MS characterization (**Figure S12**). In addition to direct quantitative analysis of the whole region of interest, the evolution of local W-element content in each pixel would provide additional insights into the metal dissolution-redeposition dynamics. XFM image subtraction and subsequent pixel-by-pixel analysis are used to generate the histograms of the difference in W-element fluorescence counts in each pixel (**Figure 2d** and **S10b**), and the degree of local evolution is reflected in the width of these histograms. The wider the distribution, the more aggressive and heterogenous the dissolution-redeposition dynamics. For

both 1^{st} –3^{rd} histograms in **Figure 2d** and **S10b**, the differences in counts in each pixel are large, indicating that some regions undergo substantial metal dissolution (positive in the difference of counts), and some other regions experience redeposition (negative in the difference of counts), thus the width of the histogram is broad. However, the WO_3 electrode with the TiO_2 surface layer shows a greater shrinkage of the histogram width (31^{st} – 33^{rd} histogram in **Figure 2d**) after 3,000 CV cycling. This is direct evidence that the *in situ* formed amorphous TiO_2 surface layer can stabilize the local dissolution-redeposition dynamics under electrochemical conditions.

The stabilizing effect of the surface layer is related to the intertwined dissolution and redeposition of the surface layer and the electrode. During 3,000 CV cycling, the TiO_2 surface layer gradually dissolves (**Figure S7)** and redeposits (**Figure S13**), but the homogeneity of Ti/(Ti+W) weight ratio distribution maintains (**Figure 2e**). In addition, we have demonstrated that the WO_3 electrode tends to form nanoflakes after 3,000 CV cycling in the 0.5 M H_2SO_4 electrolyte due to the aggressive WO_3 dissolution and redeposition.[20] However, the presence of the TiO_2 surface layer significantly changes the final electrode morphology (**Figure 2f**). The slowest CV scan rate in the 0.1 M $TiOSO_4$ + 0.5 M H_2SO_4 electrolyte will produce the thickest TiO_2 surface layer (**Table S1**). The thicker the TiO_2 surface layer, the less nanoflake formation after cycling, suggesting the greater interaction between the dissolved Ti cations and W cations. Similarly, when the WO_3 electrode directly experiences 3,000 CV cycling in 0.1 M $TiOSO_4$ + 0.5 M H_2SO_4 electrolyte, no nanoflakes can be formed (**Figure S14**). Such interaction is demonstrated by the color change of the electrolyte (**Figure S15**). When cycling the WO_3 electrode in the 0.1 mM $TiOSO_4$ + 0.5 M H_2SO_4 electrolyte, the electrolyte gradually turns yellowish. The intentionally

added Ti cations interact with the dissolved W cations and sulfate anions to form mixed complexes, which exhibit additional light absorption at 450 nm (**Figure S15**). When Ti cations come from the dissolution of the TiO_2 surface layer, similar complexes can form. Since the newly formed complexes have different deposition kinetics, the redeposition process is moderated, resulting in different electrode morphologies (**Figure 2f**). Concurrently, the concentration of dissolved W cations at the interface becomes stabilized, which can facilitate establishing the dissolution-redeposition equilibrium, thereby minimizing metal dissolution. Based on the above discussions, the intertwined dissolution-redeposition of the TiO_2 surface layer and the WO_3 electrode is the fundamental mechanism that regulates the interfacial reaction, leading to less metal dissolution in the acidic electrolyte.

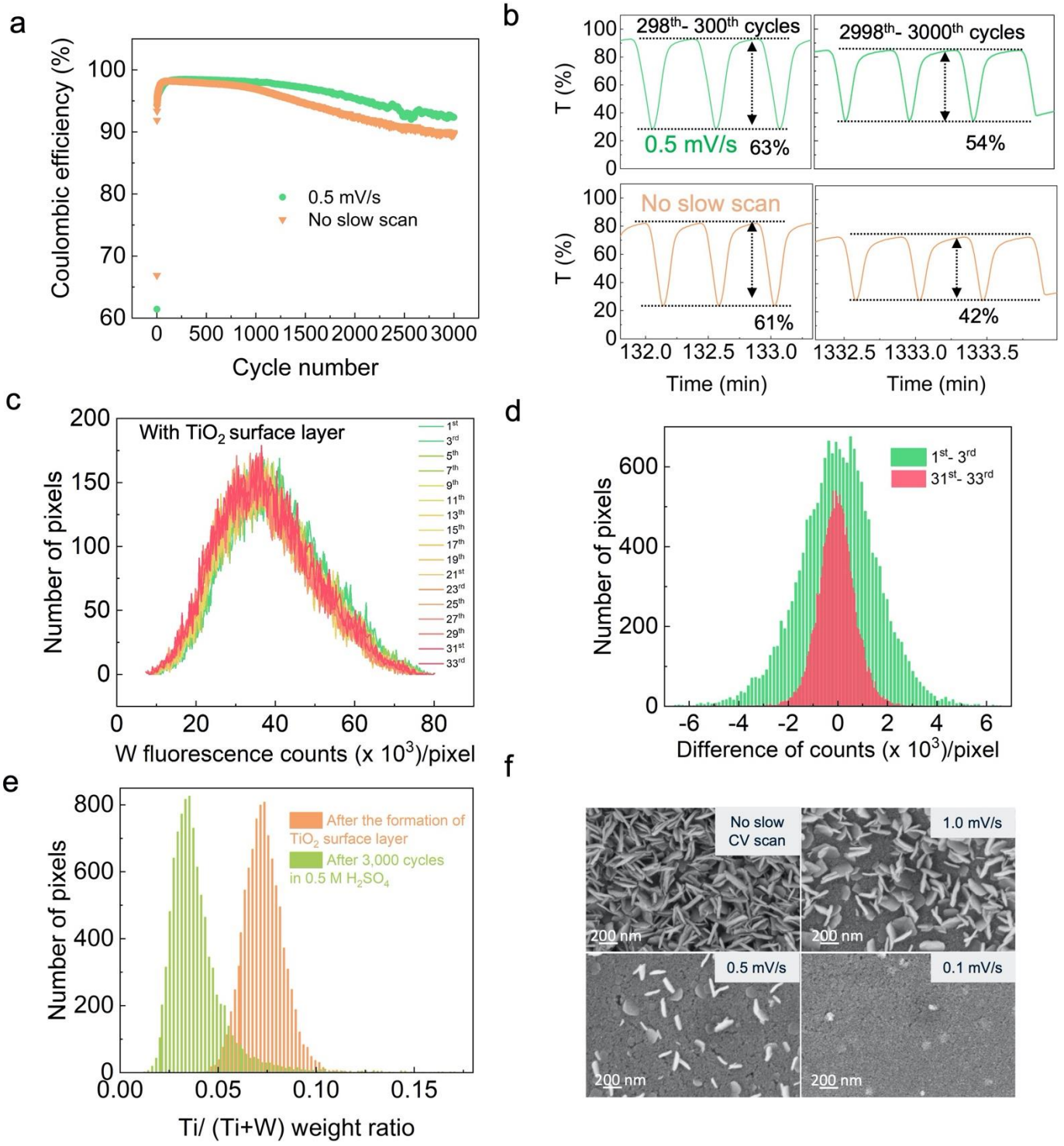

Figure 2 The alleviated dissolution of the WO_3 electrode after the formation of the amorphous TiO_2 surface layer. (a) Coulombic efficiency of the WO_3/FTO electrode during 3,000 CV cycles in 0.5 M H_2SO_4 electrolyte at 60 mV/s scan rate with -0.165 V-0.635 V vs. Ag/AgCl

(3M, NaCl). 0.5 mV/s refers to the formation of an amorphous TiO_2 surface layer with 0.5 mV/s slow scan in 0.1 M $TiOSO_4$ + 0.5 M H_2SO_4 electrolyte. No slow-scan refers to the controlled sample without the TiO_2 surface layer. (b) Optical modulation of the WO_3/FTO electrode during 3,000 CV cycles. (c) W elemental distribution curves of the W-element fluorescence counts/pixel (pixel size: 1 μm x 1 μm, X-axis) and the number of pixels (Y-axis) during 3,000 CV cycling in the 0.5 M H_2SO_4 electrolyte at 60 mV/s scan rate with -0.165 V-0.635 V vs. Ag/AgCl (3M, NaCl). The total image size is 150 μm x 110 μm with a total of 16,500 pixels. The 1st W elemental distribution curve is the first one during 3,000 CV cycling. (d) Quantitative analysis of the evolution of local W content in each pixel with the TiO_2 surface layer. 1st – 3rd represents using the 1st XFM image to subtract the 3rd XFM image. (e) *Ex situ* XFM quantitative analysis of Ti/ (Ti+ W) weight ratio of the WO_3/FTO electrode after 3 CV cycles in the 0.1 M $TiOSO_4$ + 0.5 M H_2SO_4 electrolyte at 0.1 mV/s scan rate with -0.165 V-0.635 V vs. Ag/AgCl (3M, NaCl) and its evolution after 3,000 CV cycling in 0.5 M H_2SO_4 electrolyte at 60 mV/s scan rate within the same potential range. (f) Different morphological evolutions of the electrode after 3 slow CV cycles in the 0.1 M $TiOSO_4$ + 0.5 M H_2SO_4 electrolyte (0, 0.1, 0.5, and 1.0 mV/s scan rates, respectively) and subsequent 3,000 CV cycling in the 0.5 M H_2SO_4 electrolyte (all 60 mV/s). Details of SEM images are provided in the experimental section.

The dynamic interaction between the electrode and the surface layer during electrochemical cycling exists not only when the surface layer is formed by electrochemical cycling. Another thin film deposition technique such as ALD (Atomic Layer Deposition) is used to prepare a surface

layer and it exhibits a significant evolution of elemental distribution and drastic phase transformation. Ti L-edge s-XAS results suggest that the ALD-made nominal 2 nm TiO_2 surface layer has an anatase crystalline structure,[23] but after 3,000 CV cycling in the 0.5 M H_2SO_4 electrolyte, it transforms to an amorphous structure (**Figure 3a**). The dissolution of the ALD-TiO_2 surface layer (**Figure S16**) and its interaction with the dissolved WO_3 electrode (**Figure S17a**) resulted in the dissolution of W species initially slow and then faster (**Figure S17b**). After cycling, there is no nanoflake formation (**Figure S18**). More importantly, the heterogeneity of Ti/(Ti+W) weight ratio distribution is greatly alleviated (**Figure 3b**). Since the apparent H^+ diffusion coefficient in the anatase TiO_2 layer is lower than that in the amorphous one[27] and dissolving the TiO_2 surface layer exposes more proton-intercalation WO_3 electrodes, the electrochemical capacity decays, stabilizes, and increases over cycling, while the Coulombic efficiency reduces after 1,500 cycles due to proton trapping in both amorphous TiO_2 surface layer and bulk WO_3 lattice (**Figure 3c).**[20] Concurrently, the heterogeneous, crystalline TiO_2 islands on the WO_3 electrode are transformed into a homogenous, amorphous coating layer (**Figure 3d**). The higher elemental homogeneity of the surface layer resulting from electrochemical cycling can potentially be utilized to obtain conformal surface coatings with precisely controlled chemical compositions. Altogether, the dynamic structural evolution of the surface layer during electrochemical reactions is accompanied by the dissolution and redeposition, evolution of elemental distribution, and phase transformation. These are the foundational factors that how the surface layer modulates electrochemical reactions in aqueous electrolytes by resynthesizing electrode surface chemistry.

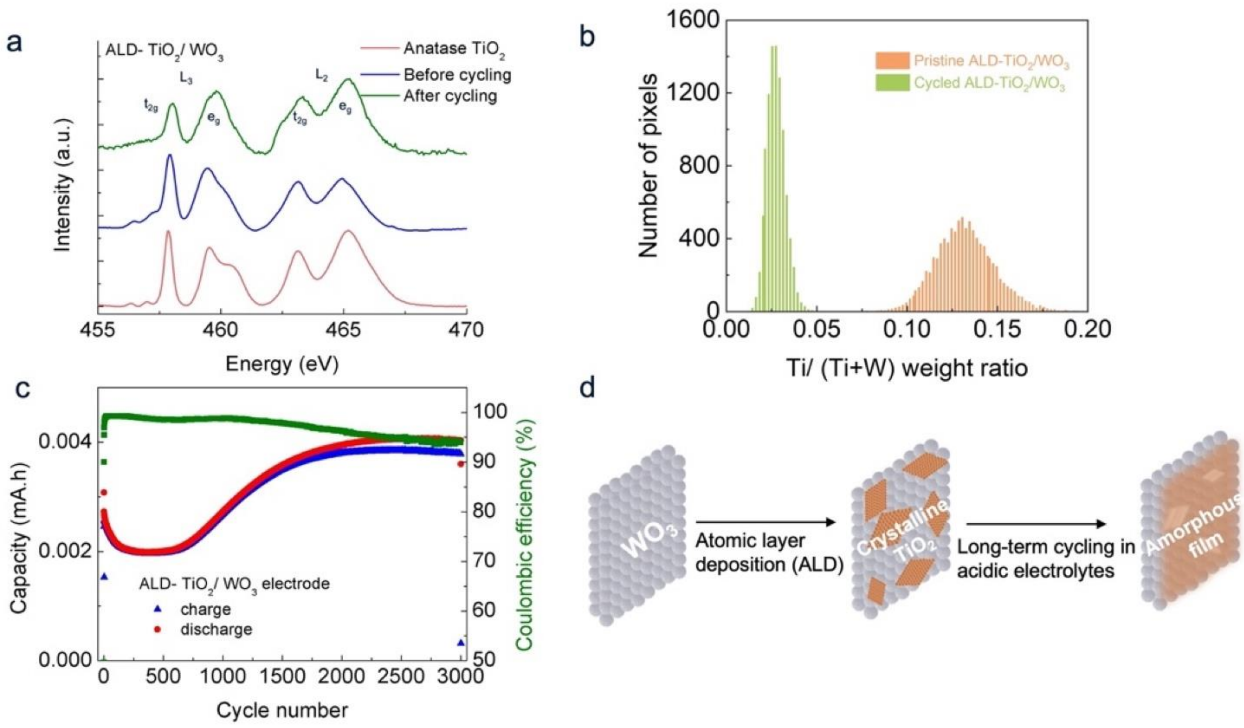

Figure 3 Structural evolution of ALD-made TiO_2 surface coating. (a) Ti L-edge s-XAS in the TEY (total electron yield) mode of the ALD-made TiO_2/ WO_3 electrode before and after 3,000 CV cycling in 0.5 M H_2SO_4 electrolyte at 60 mV/s scan rate with -0.165 V-0.635 V vs. Ag/AgCl (3M, NaCl). (b) *Ex situ* XFM quantitative analysis of Ti/(Ti+ W) weight ratio of the ALD-made TiO_2/WO_3 electrode before and after 3,000 CV cycling. (c) The electrochemical capacity evolution of the ALD-made TiO_2/WO_3 electrode during the 3,000 CV cycling. (d) Schematic illustration of the structural evolution of the ALD-made TiO_2 surface layer during electrochemical cycling: from crystalline to amorphous phase transformation and progressively uniform element distribution.

Understanding the structural and chemical evolution of the surface layer on electrodes can offer mechanistic insights into controlling the reactive electrochemical interface and enhancing our capability to manipulate electrochemical processes. The present study highlights that the solid-

liquid electrochemical interface offers a two-dimensional, geometrically confined reactive environment for the *in situ* resynthesis of electrode surface chemistry. At low CV scan rates, Ti^{4+} cations in the proton electrolyte can participate in the dissolution-redeposition dynamics at the electrochemical interface, resulting in the formation of an amorphous TiO_2 surface layer on the WO_3 electrode. Upon prolonged electrochemical cycling in the proton electrolyte, the dissolution-redeposition dynamics of the newly formed TiO_2 surface layer intertwine with those of the WO_3 electrode. Such intertwinement leads to the establishment of the dissolution-redeposition equilibrium, which inhibits metal dissolution, stabilizes electrode morphology, and promotes electrochemical performance. We further discover that a crystalline TiO_2 surface layer deposited on the WO_3 electrode can rapidly transform into an amorphous TiO_2 surface layer due to the dissolution-redeposition dynamics. In summary, our work demonstrates the dynamic nature of the metal dissolution and deposition behaviors, which can be engineered to resynthesize electrode surface chemistry and regulate electrochemical reactions at the solid-liquid interfaces.

Supporting Information Available: Experimental methods; Cyclic-Voltammetry (CV) electrochemical test of the WO_3/FTO electrode at various scan rates; Ti L-edge soft X-ray absorption spectroscopy (s-XAS) of the FTO substrate; High-angle annular dark-field (HAADF) STEM image and corresponding EDS elemental maps and EELS Ti L edge spectra; W elemental distribution curves; W XFM images; Quantitative analysis of the evolution of local W content; ICP results; Ti elemental distribution curves; SEM-EDS Ti elemental mapping; Transmittance

(T %) at 450 nm of the electrolyte; *Ex situ* Ti XFM images; Table of the quantified atomic ratios of Ti, W, and O.

Author Contributions

F.L. conceived and led the study. F.L. and A.H designed the experiments. A.H. performed synthesis, electrochemistry, and synchrotron experiments in the study. Y.Z. assisted the XFM experiments. S.S. and D.N, performed soft XAS measurements. F.Y. and J.G. performed ALD. L.L. assisted XFM experiments and participated in data analysis and discussion. E.M. participated in discussion and figure preparation. Q.D. participated in data discussion. S. H. performed electron microscopy measurement and participate in data discussion. A.H. and F.L. analyzed the data and wrote the manuscript. All authors have approved the final draft of the manuscript.

Notes

The authors declare no competing financial interests.

Acknowledgments

The work was supported by the National Science Foundation under no. CBET 1912885. Use of the Stanford Synchrotron Radiation Lightsource, SLAC National Accelerator Laboratory, is supported by the U.S. Department of Energy, Office of Science, Office of Basic Energy Sciences, under Contract No. DE-AC02-76SF00515. S. S. acknowledged funding from the Walter Ahlström Foundation and received funding from the European Union's Horizon 2020 research and

innovation programme under the Marie Skłodowska-Curie grant agreement No 841621. This research used resources of the Advanced Photon Source, which is a U.S. Department of Energy (DOE) Office of Science User Facility operated for the DOE Office of Science by Argonne National Laboratory under Contract No. DE-AC02-06CH11357. This research used resources of the Center for Functional Nanomaterials (CFN), which is a U.S. Department of Energy Office of Science User Facility, at Brookhaven National Laboratory under Contract No. DE-SC0012704. Q.D. was supported by the National Science Foundation under no. CBET 1912876. This research was partially supported by Virginia Tech's Institute for Critical Technology and Applied Science through instruments provided by the Nanoscale Characterization and Fabrication Laboratory (NCFL).

References

1. Sood, A.; Poletayev, A. D.; Cogswell, D. A.; Csernica, P. M.; Mefford, J. T.; Fraggedakis, D.; Toney, M. F.; Lindenberg, A. M.; Bazant, M. Z.; Chueh, W. C., Electrochemical ion insertion from the atomic to the device scale. *Nat Rev Mater* **2021,** *6* (9), 847-867.
2. Huggins, R., *Advanced batteries: materials science aspects*. Springer Science & Business Media: 2008.
3. Bae, D.; Seger, B.; Vesborg, P. C. K.; Hansen, O.; Chorkendorff, I., Strategies for stable water splitting via protected photoelectrodes. *Chem Soc Rev* **2017,** *46* (7), 1933-1954.
4. Yang, L. Y.; Yang, K.; Zheng, J. X.; Xu, K.; Amine, K.; Pan, F., Harnessing the surface structure to enable high-performance cathode materials for lithium-ion batteries. *Chem Soc Rev* **2020,** *49* (14), 4667-4680.
5. Asl, H. Y.; Manthiram, A., Reining in dissolved transition-metal ions. *Science* **2020,** *369* (6500), 140-141.
6. Kim, Y. J.; Cho, J. P.; Kim, T. J.; Park, B., Suppression of cobalt dissolution from the LiCoO2 cathodes with various metal-oxide coatings. *J Electrochem Soc* **2003,** *150* (12), A1723-A1725.
7. Zhang, X. D.; Shi, J. L.; Liang, J. Y.; Yin, Y. X.; Zhang, J. N.; Yu, X. Q.; Guo, Y. G., Suppressing Surface Lattice Oxygen Release of Li-Rich Cathode Materials via Heterostructured Spinel Li4Mn5O12 Coating. *Adv Mater* **2018,** *30* (29), 1801751.

8. Kim, S. Y.; Ostadhossein, A.; van Duin, A. C. T.; Xiao, X. C.; Gao, H. J.; Qi, Y., Self-generated concentration and modulus gradient coating design to protect Si nano-wire electrodes during lithiation. *Phys Chem Chem Phys* **2016,** *18* (5), 3706-3715.
9. Li, H. Q.; Zhou, H. S., Enhancing the performances of Li-ion batteries by carbon-coating: present and future. *Chem Commun* **2012,** *48* (9), 1201-1217.
10. Li, X. F.; Liu, J.; Banis, M. N.; Lushington, A.; Li, R. Y.; Cai, M.; Sun, X. L., Atomic layer deposition of solid-state electrolyte coated cathode materials with superior high-voltage cycling behavior for lithium ion battery application. *Energ Environ Sci* **2014,** *7* (2), 768-778.
11. Chen, Z. H.; Qin, Y.; Amine, K.; Sun, Y. K., Role of surface coating on cathode materials for lithium-ion batteries. *J Mater Chem* **2010,** *20* (36), 7606-7612.
12. Ma, L.; Nuwayhid, R. B.; Wu, T. P.; Lei, Y.; Amine, K.; Lu, J., Atomic Layer Deposition for Lithium-Based Batteries. *Adv Mater Interfaces* **2016,** *3* (21), 1600564.
13. Gauthier, M.; Carney, T. J.; Grimaud, A.; Giordano, L.; Pour, N.; Chang, H. H.; Fenning, D. P.; Lux, S. F.; Paschos, O.; Bauer, C.; Magia, F.; Lupart, S.; Lamp, P.; Shao-Horn, Y., Electrode-Electrolyte Interface in Li-Ion Batteries: Current Understanding and New Insights. *J Phys Chem Lett* **2015,** *6* (22), 4653-4672.
14. Stamenkovic, V. R.; Strmcnik, D.; Lopes, P. P.; Markovic, N. M., Energy and fuels from electrochemical interfaces. *Nat Mater* **2017,** *16* (1), 57-69.
15. Dunwell, M.; Yang, X.; Setzler, B. P.; Anibal, J.; Yan, Y. S.; Xu, B. J., Examination of Near-Electrode Concentration Gradients and Kinetic Impacts on the Electrochemical Reduction of CO2 using Surface-Enhanced Infrared Spectroscopy. *Acs Catal* **2018,** *8* (5), 3999-4008.
16. Ryu, J.; Surendranath, Y., Polarization-Induced Local pH Swing Promotes Pd-Catalyzed CO2 Hydrogenation. *J Am Chem Soc* **2020,** *142* (31), 13384-13390.
17. Wang, Y. Q.; Guo, L.; Guo, Y. G.; Li, H.; He, X. Q.; Tsukimoto, S.; Ikuhara, Y.; Wan, L. J., Rutile-TiO2 Nanocoating for a High-Rate Li4Ti5O12 Anode of a Lithium-Ion Battery. *J Am Chem Soc* **2012,** *134* (18), 7874-7879.
18. Li, Q.; Fu, J. J.; Zhu, W. L.; Chen, Z. Z.; Shen, B.; Wu, L. H.; Xi, Z.; Wang, T. Y.; Lu, G.; Zhu, J. J.; Sun, S. H., Tuning Sn-Catalysis for Electrochemical Reduction of CO2 to CO via the Core/Shell Cu/SnO2 Structure. *J Am Chem Soc* **2017,** *139* (12), 4290-4293.
19. Kuai, C. G.; Xi, C.; Hu, A. Y.; Zhang, Y.; Xu, Z. R.; Nordlund, D.; Sun, C. J.; Cadigan, C. A.; Richards, R. M.; Li, L. X.; Dong, C. K.; Du, X. W.; Lin, F., Revealing the Dynamics and Roles of Iron Incorporation in Nickel Hydroxide Water Oxidation Catalysts. *J Am Chem Soc* **2021,** *143* (44), 18519-18526.
20. Hu, A. Y.; Jiang, Z. S.; Kuai, C. G.; McGuigan, S.; Nordlund, D.; Liu, Y. J.; Lin, F., Uncovering phase transformation, morphological evolution, and nanoscale color heterogeneity in tungsten oxide electrochromic materials. *J Mater Chem A* **2020,** *8* (38), 20000-20010.
21. Sun, W.; Wang, F.; Hou, S. Y.; Yang, C. Y.; Fan, X. L.; Ma, Z. H.; Gao, T.; Han, F. D.; Hu, R. Z.; Zhu, M.; Wang, C. S., Zn/MnO2 Battery Chemistry With H+ and Zn2+ Coinsertion. *J Am Chem Soc* **2017,** *139* (29), 9775-9778.
22. Kelsall, G. H.; Robbins, D. J., Thermodynamics of Ti-H2O-F(-Fe) systems at 298 K. *Journal of Electroanalytical Chemistry and Interfacial Electrochemistry* **1990,** *283* (1), 135-157.

23. Kucheyev, S. O.; van Buuren, T.; Baumann, T. F.; Satcher, J. H.; Willey, T. M.; Meulenberg, R. W.; Felter, T. E.; Poco, J. F.; Gammon, S. A.; Terminello, L. J., Electronic structure of titania aerogels from soft x-ray absorption spectroscopy. *Phys Rev B* **2004,** *69* (24), 245102.
24. Kuai, C. G.; Xu, Z. R.; Xi, C.; Hu, A. Y.; Yang, Z. J.; Zhang, Y.; Sun, C. J.; Li, L. X.; Sokaras, D.; Dong, C. K.; Qiao, S. Z.; Du, X. W.; Lin, F., Phase segregation reversibility in mixed-metal hydroxide water oxidation catalysts. *Nat Catal* **2020,** *3* (9), 743-753.
25. Mu, L. Q.; Kan, W. H.; Kuai, C. G.; Yang, Z. J.; Li, L. X.; Sun, C. J.; Sainio, S.; Avdeev, M.; Nordlund, D.; Lin, F., Structural and Electrochemical Impacts of Mg/Mn Dual Dopants on the LiNiO2 Cathode in Li-Metal Batteries. *Acs Appl Mater Inter* **2020,** *12* (11), 12874-12882.
26. Wu, D. R.; Housel, L. M.; Kim, S. J.; Sadique, N.; Quilty, C. D.; Wu, L. J.; Tappero, R.; Nicholas, S. L.; Ehrlich, S.; Zhu, Y. M.; Marschilok, A. C.; Takeuchi, E. S.; Bock, D. C.; Takeuchi, K. J., Quantitative temporally and spatially resolved X-ray fluorescence microprobe characterization of the manganese dissolution-deposition mechanism in aqueous Zn/alpha-MnO2 batteries. *Energ Environ Sci* **2020,** *13* (11), 4322-4333.
27. Fang, H. T.; Liu, M.; Wang, D. W.; Sun, T.; Guan, D. S.; Li, F.; Zhou, J. G.; Sham, T. K.; Cheng, H. M., Comparison of the rate capability of nanostructured amorphous and anatase TiO2 for lithium insertion using anodic TiO2 nanotube arrays. *Nanotechnology* **2009,** *20* (22), 225701.